



HAL
open science

Modeling of 3D moisture distribution in heated concrete: From continuum towards mesoscopic approach

Dorjan Dauti, Stefano Dal Pont, Matthieu Briffaut, Benedikt Weber

► To cite this version:

Dorjan Dauti, Stefano Dal Pont, Matthieu Briffaut, Benedikt Weber. Modeling of 3D moisture distribution in heated concrete: From continuum towards mesoscopic approach. *International Journal of Heat and Mass Transfer*, 2019, 134, pp.1137-1152. 10.1016/j.ijheatmasstransfer.2019.02.017 . hal-04346885

HAL Id: hal-04346885

<https://hal.science/hal-04346885>

Submitted on 2 Feb 2024

HAL is a multi-disciplinary open access archive for the deposit and dissemination of scientific research documents, whether they are published or not. The documents may come from teaching and research institutions in France or abroad, or from public or private research centers.

L'archive ouverte pluridisciplinaire **HAL**, est destinée au dépôt et à la diffusion de documents scientifiques de niveau recherche, publiés ou non, émanant des établissements d'enseignement et de recherche français ou étrangers, des laboratoires publics ou privés.

Modeling of 3D moisture distribution in heated concrete: from continuum towards mesoscopic approach

Dorjan Dauti^{a,b}, Stefano Dal Pont^{a,*}, Matthieu Briffaut^a, Benedikt Weber^b

^a*Université Grenoble Alpes, CNRS, Grenoble INP, 3SR, 38000 Grenoble, France*

^b*Empa, Swiss Federal Laboratories for Materials Science and Technology, Überlandstrasse 129, 8600 Dübendorf, Switzerland*

Abstract

The exposure of concrete to fire, which often leads to spalling, is a phenomenon that is not yet fully understood. Given the complexity of the thermo-hydro-mechanical phenomena and their strong interaction, a combined numerical-experimental approach is indispensable for understanding the behaviour of concrete at high temperature with respect to spalling. This paper deals with the numerical modeling of moisture distribution in heated concrete, a parameter often linked with spalling, by making use of original experimental data from in-situ neutron tomography. A homogenized continuum model has been employed for investigating various aspects, such as: speed of the drying front, moisture accumulation behind this front, experimental boundary effects etc. In addition, a fully coupled 3D thermo-hydro-mechanical (THM) model on the mesoscale is presented and used for simulating an experiment with a single aggregate for the purpose of investigating the influence of the aggregate on the drying front.

Keywords: THM model, high temperature, concrete drying, mesoscopic, neutron tomography

1. Introduction

Fire spalling of concrete is a phenomenon that compromises the safety of concrete structures (*e.g.* tunnels, high-rise buildings etc.) as it exposes the reinforcement steel to high temperature and results in a reduced cross section of the concrete element. Despite the extensive research dedicated to spalling, this phenomenon is not yet fully understood due to the complex behaviour of concrete at high temperature, which involves heat and mass transfer, known as thermo-hydral (TH) processes, as well as mechanical processes. All of these physical processes are strongly coupled to each other. State-of-the-art numerical models that take into account the coupled thermo-hydro-mechanical (THM) behaviour have been presented in literature [1, 2, 3, 4]. The validation of these numerical models is usually based on experimental studies [5, 6] that monitor parameters such as gas pressure (P), temperature (T) and global mass loss (M). While such kind of experiments represent an important progress in better understanding the high temperature behaviour of concrete, they come along with some limitations due to the point-wise nature of temperature and gas pressure measurements. First, the measurements might be influenced by the embedded sensors. Second, the full-field information, which takes into account the role of concrete heterogeneity, is missing.

In addition to PTM tests, neutron radiography has been employed for investigating the physical processes in heated concrete [7, 8]. Due to the high neutron attenuation coefficient of hydrogen, neutron imaging proved to be an effective method for investigating the evolution of moisture content

*Corresponding author

Email address: stefano.dalpont@3sr-grenoble.fr (Stefano Dal Pont)

in real time in concrete while being heated. The moisture profiles obtained from 2D images captured with neutron radiography have been used in Dauti et al. [9] for identifying and investigating some critical constitutive laws adopted by the state-of-the-art models for concrete at high temperature. This study showed that neutron imaging complemented with THM numerical modeling is an effective approach for adjusting the parameters of some critical constitutive laws that cannot be measured directly.

However, in neutron radiography, the attenuation coefficient is averaged over the thickness of the sample. In other words, information is available only in 2D and the mesoscale information is missing. Recently, Dauti et al. [10] performed in-situ neutron tomography experiments for measuring the distribution of moisture content in 3D. Local information obtained in this experimental study provided valuable insight on several aspects, such as: (i) the influence of the aggregates on the evolution of the moisture content, (ii) moisture accumulation behind the drying front, (iii) additional lateral drying of the heated specimens despite the precautions taken using the standard heat and moisture isolation techniques.

These original experimental data are used for the first time in this paper to support the results of a thermo-hydro-mechanical model that describes the high-temperature behaviour of concrete. The first objective of the paper is verifying that the THM model with adjusted constitutive laws from a previous study [9] is able to predict the temperature and 3D moisture distribution given by neutron tomography. The second objective is studying the influence of the experimental boundary condition on the moisture distribution using the numerical model. The final objective is investigating the influence of aggregates on drying of concrete. For that purpose, a 3D mesoscale model that takes into account explicitly the concrete components (aggregates, cementitious matrix etc.), in other words the heterogeneity of concrete, is needed. In literature, Xotta et al. [11] have presented a THM model in the mesoscale. However, in that study the transport phenomena in concrete are described by a single fluid phase model. In the present study, a full multiphase THM coupled model will be used for performing mesoscopic analyses.

In Section 2, the neutron tomography experimental data that have been used in this study for verification of the numerical model are summarized. In Section 3, the mathematical model used for simulating the behavior of concrete as a homogeneous (Section 3.1) but also as a heterogeneous material (Section 3.2) is presented. Then, in Section 4, the numerical analysis is presented. First, in Section 4.3, a 2D homogenized continuum model is used for simulating the temperature and moisture distribution measured experimentally. Next, in Section 4.4, 3D simulations using a homogenized continuum model (see in Section 4.4.1) as well as a mesoscopic modelling strategy for performing a simplified mesoscopic analysis for investigating the influence of an aggregate on the drying front (see in Section 4.4.2) are presented.

2. Neutron tomography experiments

Neutron tomography is an innovative technique, which can provide more detailed information about local moisture distribution. The principle of neutron tomography is very similar to X-ray computed tomography. However, in contrast to X-rays which interact with electrons and whose attenuation thus depends on the atomic number, neutrons interact with the nuclei. The hydrogen atoms of the water molecules highly attenuate neutrons, which makes it possible to detect the moisture and drying front in concrete. In addition, due to the presence of free and chemically bound water, the cement paste has higher neutron attenuation than the aggregates. Thus, the latter can be easily distinguished from the cement matrix.

The experiments performed by Dauti et al. [10] consisted of heating tests performed inside a neutron beamline for the purpose of tracking the evolution of the moisture content while concrete was being exposed to high temperature. Cylindrical specimens with diameter 3 cm were tested. As one of

the objectives was to estimate the influence of the aggregate size, two concrete mixes (see Table 1) were used: one with maximum aggregate size of 4 mm (HPC 4 mm) and the other with 8 mm (HPC 8 mm). The overall volume of aggregates was the same for both mixes. In addition, a sample HPC 4 mm with a single aggregate near the heated surface was cast for a more direct investigation of the influence of the aggregate on the moisture migration. The samples HPC 8 mm and HPC 4 mm were equipped with thermocouples at 3, 10, and 20 mm depth for temperature measurements. For maximizing the unidimensionality of the heat and mass transfer, the samples were insulated laterally with self adhesive aluminium tape and rockwool.

A drawing of the heating cell is shown in Figure 1. Each sample was placed inside the heating cell and heated on the top face during 1 hr using a radiant heater which reached 500°C. The heater is placed in a cover on top of the cell consisting of an aluminium tube, which is rather transparent to neutrons. At the bottom of the heating cell, the specimen stands on a cement fiberboard, which is also used for thermal insulation.

While the sample was being heated, neutron tomography was performed, as shown in Figure 2, for measuring in real time the moisture distribution in 3D. During the heating test, 60 tomographies (3D scans) were taken. Each tomography, which comprised 500 projections, was acquired in only one minute. Such acquisition time was fast enough for following the rapid dehydration process in concrete.

	HPC 4 mm	HPC 8 mm
Cement CEM I 52.5 R	488	488
Silica fume	122	122
Aggregate 0–1 mm	632.8	400
Aggregate 1–4 mm	949.2	600
Aggregate 4–8 mm	0	582
Superplasticizer SIKA 20HE	8.54	8.54
Water	189.1	189.1
w/b total	0.31	0.31

Table 1: Concrete mixtures [kg/m³]

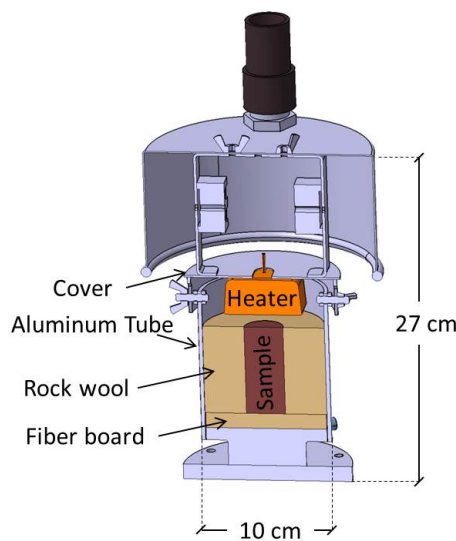


Figure 1: Drawing of the heating cell

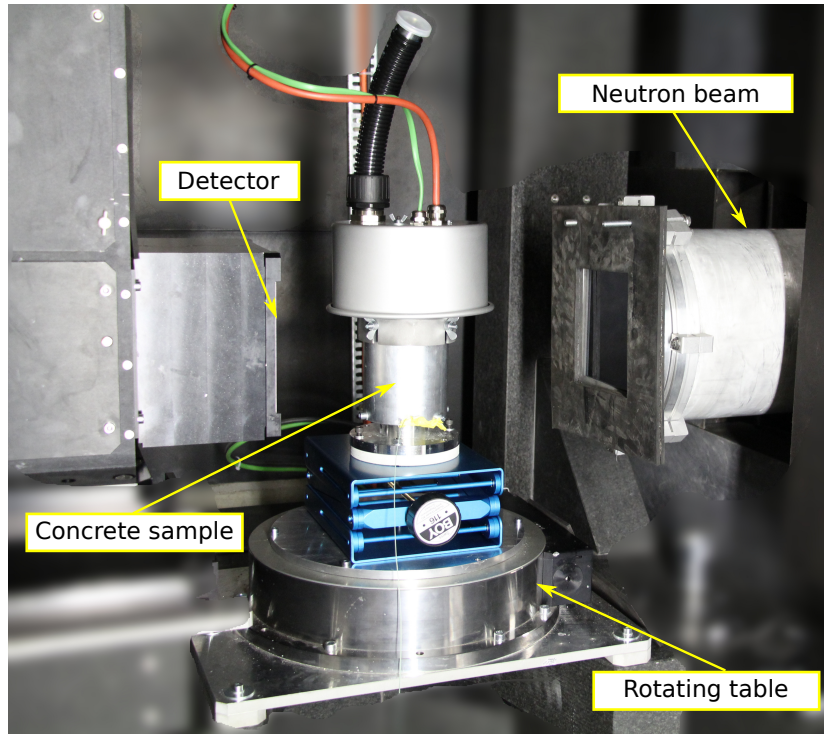


Figure 2: Setup in the NeXT(D50) beamline at Institute Laue Langevin (ILL)

In Figure 3, vertical slices from 3D scans at three different times containing the samples' axis of rotation are shown for three tested samples: HPC 8 mm (left), HPC 4 mm (middle), HPC 4 mm with a single big aggregate at the top (right). The evolution of the drying front is evident in the images. These results show qualitatively how the drying front moves faster in the sample HPC 8 mm compared to HPC 4 mm. They also show how a single aggregate severely affects the test, accelerating the drying process and modifying its shape.

A possible explanation of the differences in the drying front is heat-induced cracking and its dependency on the aggregate size. The more pervasive fracture network induced around the bigger aggregates would accelerate the drying process. The direct proof of this more pervasive fracture network was not possible by neutron imaging since the pixel size $200\ \mu\text{m}$ is not sufficient for detecting microcracks.

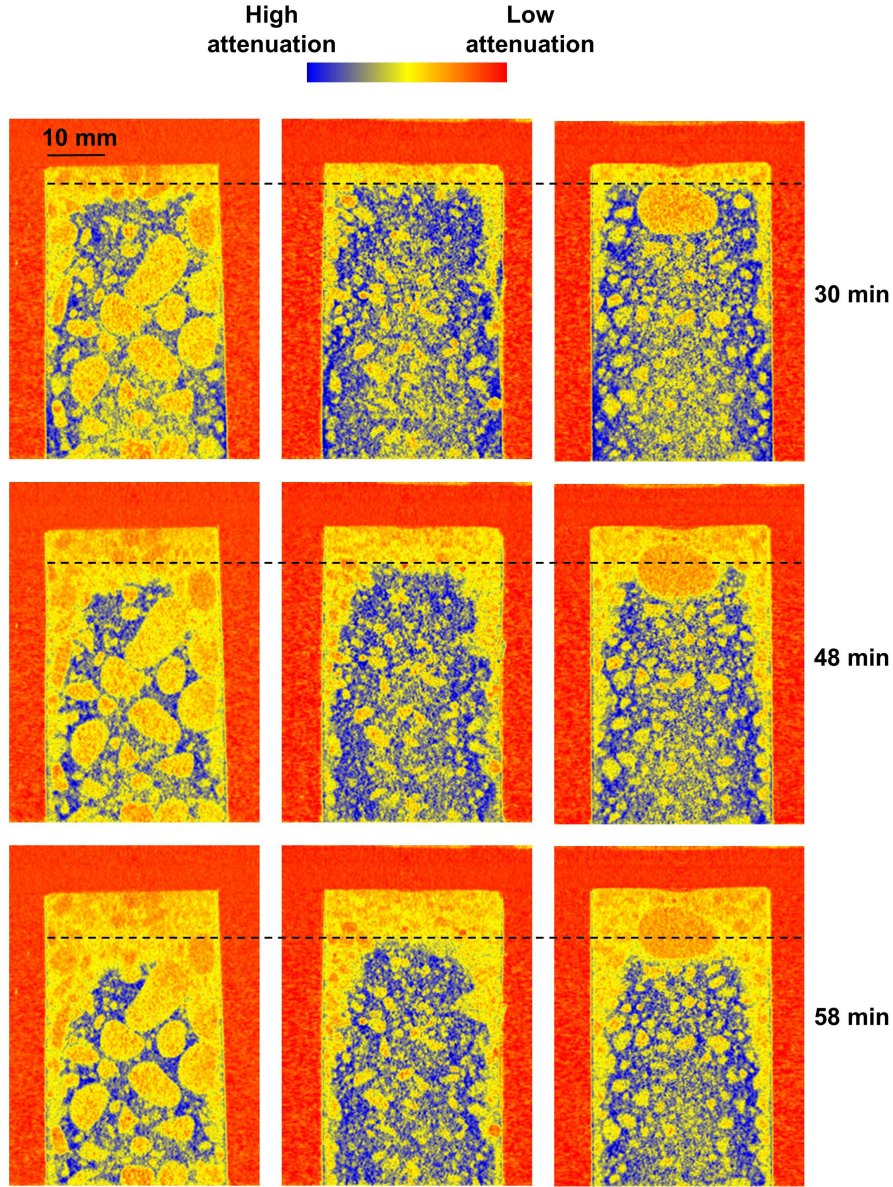


Figure 3: Vertical slices from reconstructed 3D volumes showing the evolution of the drying front in HPC 8 mm (on the left), HPC 4 mm (in the middle) and HPC 4 mm with a single aggregate (on the right)

Another highlighted information is that, in all tested samples, there was additional drying at the lateral boundaries. This indicates that the heat and/or moisture isolation methods (rock wool for heat and aluminium foil for moisture), which were employed and are conforming to the standard procedures usually used in high-temperature experiments, need to be improved.

3. Mathematical Model

3.1. Homogenized Continuum Model

In this section, a homogenized continuum model, which has been used in this paper for simulating the high temperature behaviour of concrete, is presented. The model is based on the hybrid mixture theory in the mathematical formulation originally proposed in Hassanizadeh and Gray [12, 13, 14] and then applied for geomaterials in [15], and for building materials in [1]. For sake of brevity, only the final form of the macroscopic conservation equations is given here. The full development of the model equations starting from the local microscopic balance equations with successive volume averaging can be found in [15, 16, 17, 18].

3.1.1. Conservation Equations

The model consist of 4 conservation equations: mass conservation of dry air, mass conservation of water species, energy conservation, and linear momentum conservation. For describing the state of concrete at high temperature, 4 primary variables are chosen: gas pressure p_g , capillary pressure p_c , temperature T , and displacement vector \mathbf{u} . The model equations are developed with respect to the primary variables:

- Dry Air

$$\begin{aligned} \phi(1 - S_l) \left(\frac{\partial \rho_a}{\partial T} \frac{\partial T}{\partial t} + \frac{\partial \rho_a}{\partial p_c} \frac{\partial p_c}{\partial t} + \frac{\partial \rho_a}{\partial p_g} \frac{\partial p_g}{\partial t} \right) - \phi \rho_a \left(\frac{\partial S_l}{\partial T} \frac{\partial T}{\partial t} + \frac{\partial S_l}{\partial p_c} \frac{\partial p_c}{\partial t} \right) \\ + (1 - S_l) \rho_a \frac{\partial \phi}{\partial T} \frac{\partial T}{\partial t} - \nabla \cdot \left(K \frac{\rho_a k_{rg}}{\mu_g} \nabla p_g \right) - \nabla \cdot \left(D \rho_g \frac{M_v M_a}{M_g^2} \nabla \left(\frac{p_a}{p_g} \right) \right) = 0 \quad (1) \end{aligned}$$

- Water species

$$\begin{aligned} (S_l \rho_l - (1 - S_l) \rho_v) \frac{\partial \phi}{\partial T} \frac{\partial T}{\partial t} + S_l \phi \frac{\partial \rho_l}{\partial T} \frac{\partial T}{\partial t} + \phi (\rho_l - \rho_v) \left(\frac{\partial S_l}{\partial T} \frac{\partial T}{\partial t} + \frac{\partial S_l}{\partial p_c} \frac{\partial p_c}{\partial t} \right) \\ + (1 - S_l) \phi \left(\frac{\partial \rho_v}{\partial T} \frac{\partial T}{\partial t} + \frac{\partial \rho_v}{\partial p_c} \frac{\partial p_c}{\partial t} + \frac{\partial \rho_v}{\partial p_g} \frac{\partial p_g}{\partial t} \right) - \nabla \cdot \left(K \frac{\rho_l k_{rl}}{\mu_l} (\nabla p_g - \nabla p_c) \right) \\ - \nabla \cdot \left(K \frac{\rho_v k_{rg}}{\mu_g} \nabla p_g \right) - \nabla \cdot \left(D \rho_g \frac{M_v M_a}{M_g^2} \nabla \left(\frac{p_v}{p_g} \right) \right) = -\dot{m}_{dehyd} \quad (2) \end{aligned}$$

- Energy

$$\begin{aligned} \rho C_p \frac{\partial T}{\partial t} - K \left(C_l \frac{\rho_l k_{rl}}{\mu_l} (\nabla p_g - \nabla p_c) + C_g \frac{\rho_v k_{rg}}{\mu_g} \nabla p_g \right) \cdot \nabla T - \nabla \cdot (\lambda \cdot \nabla T) = \\ - H_{vap} \dot{m}_{vap} + H_{dehyd} \dot{m}_{dehyd} \quad (3) \end{aligned}$$

- Linear momentum

$$\nabla \cdot (\mathbf{t}^{Total}) + \rho \mathbf{g} = 0 \quad (4)$$

3.1.2. Finite element formulation and implementation

The weak form of Eqs (1 - 4) was obtained in [15, 16] and is discretized using the finite element method. The unknown variables are expressed in terms of their nodal values as:

$$p_g(t) = \mathbf{N}_{p_g} \bar{\mathbf{p}}_g(t) \quad p_c = \mathbf{N}_{p_c} \bar{\mathbf{p}}_c(t) \quad T = \mathbf{N}_T \bar{\mathbf{T}}(t) \quad \mathbf{u}(t) = \mathbf{N}_u \bar{\mathbf{u}}(t)$$

where $\bar{\mathbf{p}}_g(t)$, $\bar{\mathbf{p}}_c(t)$, $\bar{\mathbf{T}}(t)$, $\bar{\mathbf{u}}(t)$ are vectors of the nodal values of the primary variables at the time instant t , and \mathbf{N}_{p_g} , \mathbf{N}_{p_c} , \mathbf{N}_T , \mathbf{N}_u are the shape functions related to these variables. After the finite element discretization, the weak form of the final system of Eqs. (1 - 4) can be expressed in the following matrix form:

$$\mathbf{C}_{ij}(\mathbf{Y}) \frac{\partial \mathbf{Y}}{\partial t} + \mathbf{K}_{ij}(\mathbf{Y}) \mathbf{Y} = \mathbf{f}_i(\mathbf{Y}) \quad (5)$$

with:

$$\mathbf{K}_{ij} = \begin{pmatrix} \mathbf{K}_{gg} & \mathbf{K}_{gc} & \mathbf{K}_{gt} & 0 \\ \mathbf{K}_{cg} & \mathbf{K}_{cc} & \mathbf{K}_{ct} & 0 \\ \mathbf{K}_{tg} & \mathbf{K}_{tc} & \mathbf{K}_{tt} & 0 \\ \mathbf{K}_{ug} & \mathbf{K}_{uc} & \mathbf{K}_{ut} & \mathbf{K}_{uu} \end{pmatrix} \quad \mathbf{C}_{ij} = \begin{pmatrix} \mathbf{C}_{gg} & \mathbf{C}_{gc} & \mathbf{C}_{gt} & \mathbf{C}_{gu} \\ 0 & \mathbf{C}_{cc} & \mathbf{C}_{ct} & \mathbf{C}_{cu} \\ 0 & \mathbf{C}_{tc} & \mathbf{C}_{tt} & \mathbf{C}_{tu} \\ 0 & 0 & 0 & 0 \end{pmatrix} \quad \mathbf{f}_i = \begin{pmatrix} \mathbf{f}_g \\ \mathbf{f}_c \\ \mathbf{f}_t \\ \mathbf{f}_u \end{pmatrix}$$

where $\mathbf{Y} = \{\bar{\mathbf{p}}_g, \bar{\mathbf{p}}_c, \bar{\mathbf{T}}, \bar{\mathbf{u}}\}$ is the approximated solution.

The numerical implementation realized in the presented work is based on an existing implementation for concrete subject to severe loading conditions proposed in [19, 20]. In that work, the system of equations has been solved using a partitioned procedure, also known as staggered solution strategy. The latter implies that within one time step every single equation is solved for a given variable of the system while keeping the others constant. While this iterative procedure is a relatively simple and flexible strategy to solve coupled problems, it has a high computational cost due to the nested iterations that characterize the procedure. The time efficiency becomes particularly important when considering 3D problems or mesoscopic scales. Inspired by the work of Sciumé [21], a new solution strategy has been used in the present work for implementing the thermo-hydral numerical model in the finite element software Cast3M [22]. In this new implementation, the solution of the system of equations of the TH part (thermo-hydral) is obtained by adopting a fully coupled monolithic approach. In contrast to the staggered approach, a new finite element (see Figure 4) allows computing the three primary variables at each node in the same time loop, so only one level of iteration is required. A faster convergence is achieved thanks to the monolithic system. This reduces significantly (20-30 times) the computational cost compared to the previous implementation. The linear momentum conservation equation can then be linked with the monolithic TH model. For a given time step, the new computed TH solution can be used to compute the mechanical solution, which then is fed back to the hydral model (*i.e.*, damage-permeability coupling). This permits having a coupled thermo-hydro-mechanical model.

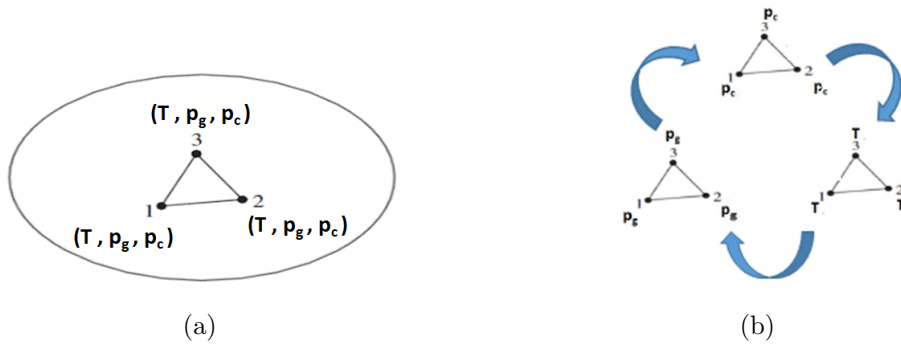


Figure 4: (a) Monolithic approach with a finite element with three unknowns in each node which are computed simultaneously, in contrast to (b) staggered approach where the sequential solution strategy is adopted

3.2. Mesoscopic Model

In order to provide a more realistic description of concrete, the numerical model has been extended to mesoscale. This numerical modeling strategy goes to the mm-cm scale considering separately the thermo-hydro-mechanical properties of each concrete constituent.

In the present work, concrete is treated as a bi-component material made of aggregates and cementitious matrix, occupying respectively the domains Ω_a and Ω_c with a perfect bond at the interface (Σ_{ac}). The interfacial transition zone is neglected. The mesoscopic modeling scheme is presented in Figure 5.

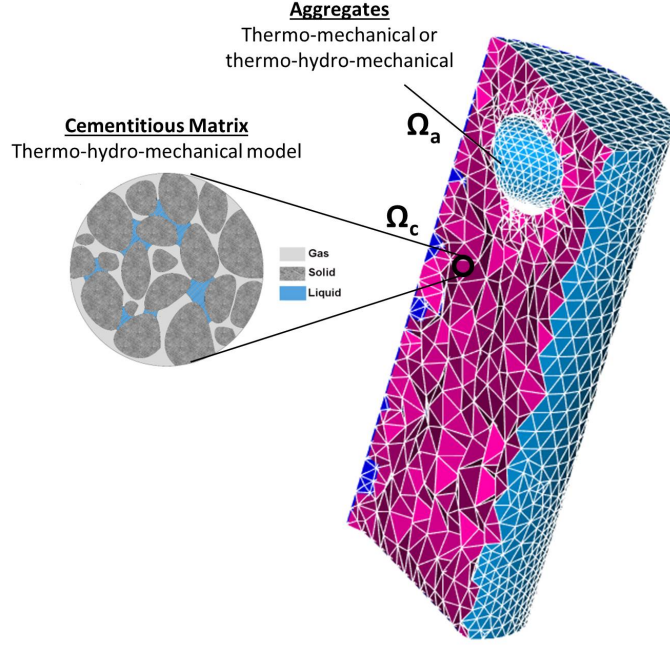


Figure 5: Mesoscale modeling scheme

An aggregate can be modeled as an impermeable solid inclusion, so a thermo-mechanical model can be adopted for the description of its behavior at high temperature, neglecting hydal effects. However, in the case of permeable aggregates, a thermo-hydro-mechanical model could be easily considered for the aggregates. The heat transfer for the domain of the aggregates Ω_a is governed by the standard energy conservation equation:

$$\rho_a C_{p_{ag}} \frac{\partial T}{\partial t} - \nabla \cdot (\lambda_{ag} \cdot \nabla T) = 0 \quad (6)$$

where ρ_{ag} is the density, $C_{p_{ag}}$ is the thermal capacity, and λ_{ag} is the thermal conductivity of aggregates. Note that this energy conservation equation is the same as the one used for a porous medium (see Equation 3) if we neglect the hydal effects. This energy equation is coupled with a mechanical model (linear elastic, damage etc), which describes the mechanical behavior of aggregates at high temperature.

It is important to note here the differences in mechanical behavior at high temperature between aggregates and cementitious matrix [6]. In contrast to the homogenized continuum models where the thermal dilation coefficient of concrete is approximated by a single linear function [23], in mesoscopic modeling the thermal behavior of each constituent has been considered explicitly.

As the aggregates normally constitute 50-80% of the total volume of concrete, their thermal dilation (β_s^{ag}) has an impact on the thermal dilation of concrete (β_s). Aggregates used in a concrete mix come usually from sedimental rocks made of silicate or calcareous, metamorphic rocks like quartz or volcanic rocks like basalts, granites etc. All of these rocks exhibit a positive thermal dilation (*i.e.*, expansion) within the temperature range of a fire incident. The thermal expansion of aggregates depends mainly on the amount of silica. Rocks with a high percentage of silica, such as quartz, exhibit a high expansion. In contrast, rocks with low (or zero) percentage of silica, such as calcareous rocks, have a lower thermal expansion [24]. For the aggregates, the thermal dilation strains are expressed as:

$$d\varepsilon_{th}^{ag} = \beta_s^{ag}(T) dT \mathbf{I} \quad (7)$$

where $\beta_s^{ag}(T)$ is the evolution of the thermal dilation coefficient of aggregates with temperature.

The cementitious matrix is considered as porous medium (solid skeleton, liquid, vapor, air), so the thermo-hydro-mechanical model, described by Equations 1-4, is used.

Concerning the thermal dilation, a study [24] on 4 different types of cement paste showed that the latter first expands, up to 150° C and then shrinks beyond this temperature. The expansion is attributed to the volumetric expansion of water molecules and to the reduction of capillary forces at higher temperatures, whereas the shrinkage is attributed to the loss of free water (evaporation) and chemically bound water (dehydration) which induce important shrinkage strains.

The temperature, at which the cement paste changes behavior (*i.e.*, from expansion to shrinkage) depends on the heating rate. Hager [25] found out that at a heating rate 1°C/min, this temperature is 120°C, whereas at a heating rate 0.5°C/min, this temperature increases to 180°C. This shows the dependence of the kinetics of dehydration on the thermal dilation of the cement paste.

The free thermal strains for the cementitious matrix can be expressed as:

$$d\varepsilon_{th}^c = \beta_s^c(T)dT \mathbf{I} \quad (8)$$

where $\beta_s^c(T)$ is the evolution of the thermal dilation coefficient of the cementitious matrix with temperature.

4. Numerical Analysis

The numerical model described in Section 3 has been used in the past for simulating standard PTM tests [26] but also moisture profiles from 2D images given by neutron radiography [9]. In the present study, the model has been employed for the simulation of temperatures and moisture profiles obtained from the neutron tomography tests presented in Section 2.

The constitutive relations and the boundary conditions used in the simulations are given in Section 4.1 and 4.2, respectively. First, a homogenized continuum model in 2D (see section 4.3) is adopted in the numerical analysis in order to verify the predicting capabilities of the model that employs some adjusted constitutive laws from a previous study [9]. Then 3D simulations using a homogenized continuum model but also a mesoscopic model are presented in Section 4.4.

4.1. Constitutive relations

Constitutive relationships describing the high-temperature behavior of concrete are needed for expressing all the components of the model equations in terms of the primary variables. These relationships include equations of state for constituents of the porous medium and material functions describing certain physical properties and their evolution with temperature. The compilation of constitutive relationships of the numerical model used in this study can be found in [27] and only some key relationships are given here.

A critical area for consideration in the model lies on some key aspects of the behaviour of concrete at high temperature described by a set of constitutive relations such as dehydration and water retention curves. The parameters of these constitutive laws can not be directly measured. However, in a previous study by Dauti et al. [9], neutron radiography complemented with numerical modeling allowed the adjustment of these constitute laws. Given the fact that the same concrete mix is being considered in the current study, these adjusted constitutive laws, presented in Figure 6, have been directly adopted for predicting the moisture profiles obtained from neutron tomography.

Another important parameter is the permeability of concrete. The discrepancy of permeability measurements for concrete at room temperature and especially for concrete at high temperature represents an important uncertainty when modeling heated concrete. In the state-of-the-art models [1], the evolution of permeability with temperature and pressure is described by the following relation:

$$k = k_0 \cdot 10^{A_T(T-T_0)} \cdot \left(\frac{p_g}{p_{atm}} \right)^{A_p} \quad (9)$$

where $A_T = 0.005$, and $A_p = 0.368$. Considering the lack of permeability measurements on the tested concrete sample but also the wide range of permeability measurements found in literature for similar type of concrete, the intrinsic value of permeability was adjusted based on the moisture profiles as explained in [9].

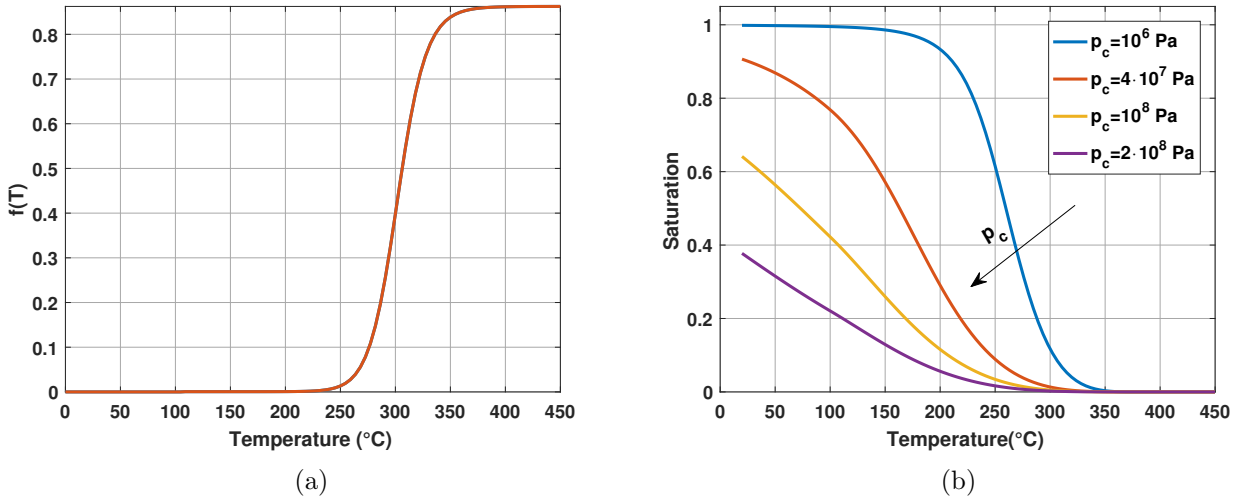


Figure 6: (a) Dehydration curve (b) Water retention curves

4.2. Boundary Conditions

The boundary conditions are schematically represented in Figure 7 (more details are given in e.g. [28]).

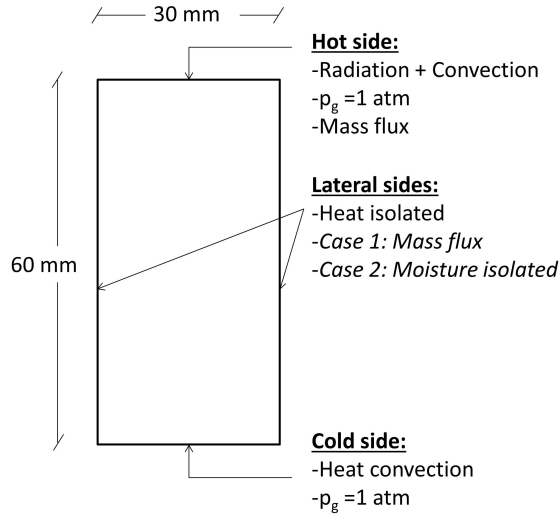


Figure 7: Boundary conditions adopted in the simulations

On the hot side, the heat flux due to radiation and convection is:

$$-\mathbf{n}(-k_{eff}\nabla T) = h_T^{hot}(T_{ext} - T) + \sigma\epsilon(T_{ext}^4 - T^4) \quad (10)$$

whereas on the cold side, heat convection with the ambient air is considered but the effect of radiation is assumed negligible:

$$-\mathbf{n}(-k_{eff}\nabla T) = h_T^{cold}(T_{ext} - T) \quad (11)$$

The averaged heat exchange coefficients, assumed to be constant during the simulations, are $h_T^{hot} = 18 \frac{\text{W}}{\text{m}^2\cdot\text{K}}$ for the hot side and $h_T^{cold} = 8 \frac{\text{W}}{\text{m}^2\cdot\text{K}}$ for the cold side, as in [1, 29, 30, 17, 16].

For the test, the radiator was heated up to 500°C within 3 min and kept at constant temperature until the end of the test. When such a heating curve is used as an external heating (T_{ext}) in Equation 10, the temperature is overestimated and the external temperature has to be reduced by 100° ($T_{ext} = 400^\circ$) for obtaining reasonable results with respect to measurements. In another numerical study in literature with similar boundary conditions [30], the authors also had to reduce T_{ext} , for reproducing the measured temperature. The reason behind the need for reducing the external temperature is probably related to some complexities at the hot boundary, *e.g.* limited surface of radiator, interaction between radiator and concrete surface (emissivity of radiator), complex air movement in the gap between the radiator and concrete surface, which are not fully considered by the boundary condition in Equation 10. However, such a thermal boundary condition that captures all the complex thermal processes falls outside the scope of this study.

For the gas mixture, the pressure is fixed at atmospheric pressure on the hot and cold sides:

$$p_g = p_{atm} \quad (12)$$

Natural boundary conditions are assumed for air at the lateral sides (no air flux).

The boundary condition for the vapor transport through the hot side is specified by the vapor flux as:

$$-\mathbf{n}(\rho_v \mathbf{v}_v + \rho_l \mathbf{v}_l) = h_m(\rho_v^{amb} - \rho_v) \quad (13)$$

where h_m is the mass transfer coefficient, assumed to be constant and equal to 0.018 m/s as in [29, 16, 20].

More critical are the boundary conditions for heat and vapor at the lateral sides. Despite the experimental precautions undertaken for obtaining a uniform (1D) drying front, an additional lateral drying was observed in all the tested samples (see Figure 3). This boundary effect could be due to lateral moisture loss and/or additional lateral heating. Samples with and without aluminium tape were tested. It has been observed from the neutron experiments that, when the samples are not wrapped with aluminium tape, drops of water are formed in the rock-wool that surrounds the sample (not necessarily close to the sample). When the sample is wrapped with aluminium tape, condensation of water seems to appear at the lateral face of the cylindrical sample (see Figure 3) but no drops of water are observed in the rock-wool. Such observation leads to the hypotheses that despite the insulation with aluminium tape, the moisture escapes laterally and travels out along the interface between the tape and the sample. The lateral drying due to the heat conduction of the tape is also possible. However, if this was the dominant effect, the specimen wrapped with aluminium tape would dry faster than the one without tape due to heat conduction. This was not the case as the experiments have shown a similar drying speed.

For modeling the additional lateral drying, a boundary condition as in Equation 13, with $h_m = 0.009 \text{ m/s}$, is applied on the lateral sides. For the purpose of investigating the influence of the boundary condition, the case with perfect lateral moisture isolation is also considered and discussed in Section 4.3.3.

4.3. 2D simulations

In this section, a 2D model has been used for simulating the measured temperature and moisture profiles. A rectangular geometry, representing the cylindrical specimen with $d = 30 \text{ mm}$ and $h = 60 \text{ mm}$, is discretized in quadrilateral finite elements with 1.5 mm size.

4.3.1. Temperature and gas pressure

In Figure 8, the temperatures obtained from the numerical model (solid lines) are compared with the experimental measurements (dashed lines) using the three thermocouples located at nominal distances 3, 10, and 20 mm from the heated surface. Note that the numerical values are evaluated at the exact position of the thermocouple welding points determined from the neutron tomography and reported in [10].

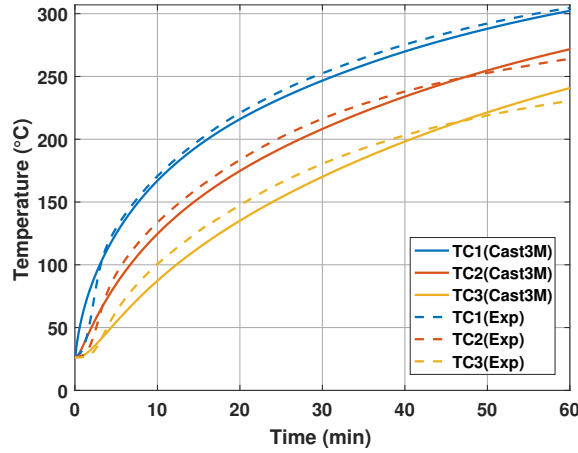


Figure 8: Simulation of the temperature profiles versus time measured by the three thermocouples (TC1, TC2, TC3) placed at three nominal positions (3, 10, and 20 mm from the heated surface)

The pressure field at different times is shown in Figure 9. The lateral boundary condition allowing for vapor transfer results in a release of pressure at the lateral sides.

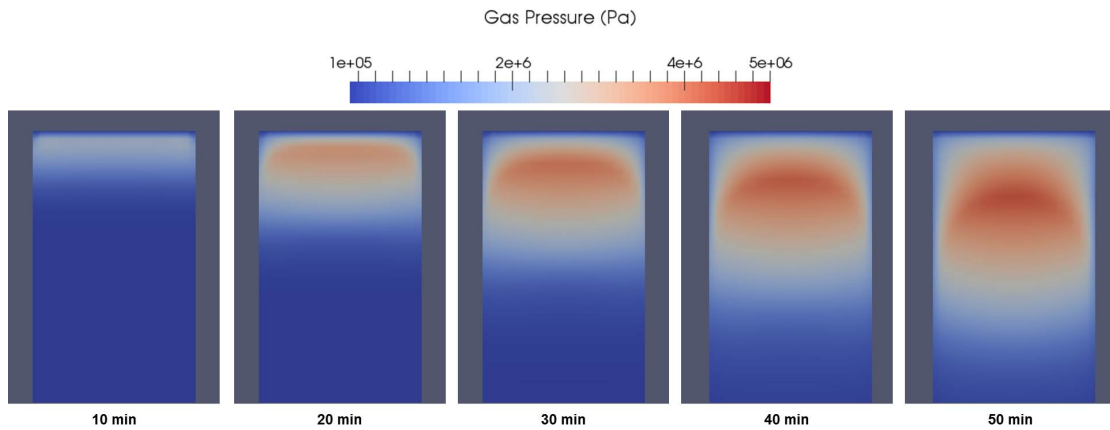


Figure 9: Pressure field highlighting its non-uniformity

4.3.2. Moisture content

When temperature increases, the moisture content in the cement paste evolves due to the physical processes of dehydration, evaporation, and condensation.

In Figure 10(a) the variation of the water content at different time steps obtained experimentally is visualized and compared with the numerical results presented in Figure 10(b). When a mass flux boundary condition is adopted, the numerical model captures the additional drying at the boundaries observed experimentally. Such results confirm the hypothesis that the boundary effect arises from an insufficient moisture insulation on the lateral surface.

A moisture accumulation can be visually observed in the numerical results in Figure 10(b) when looking at the core of the specimen (darker color). The experiments shown in Figure 10(a), on the other hand, seem to suggest drying in the core. However, this is believed to be an artefact of neutron imaging. Further image analysis, performed in [10], also showed the presence of a moisture accumulation. A quantitative comparison of this accumulation is shown and discussed in the following.

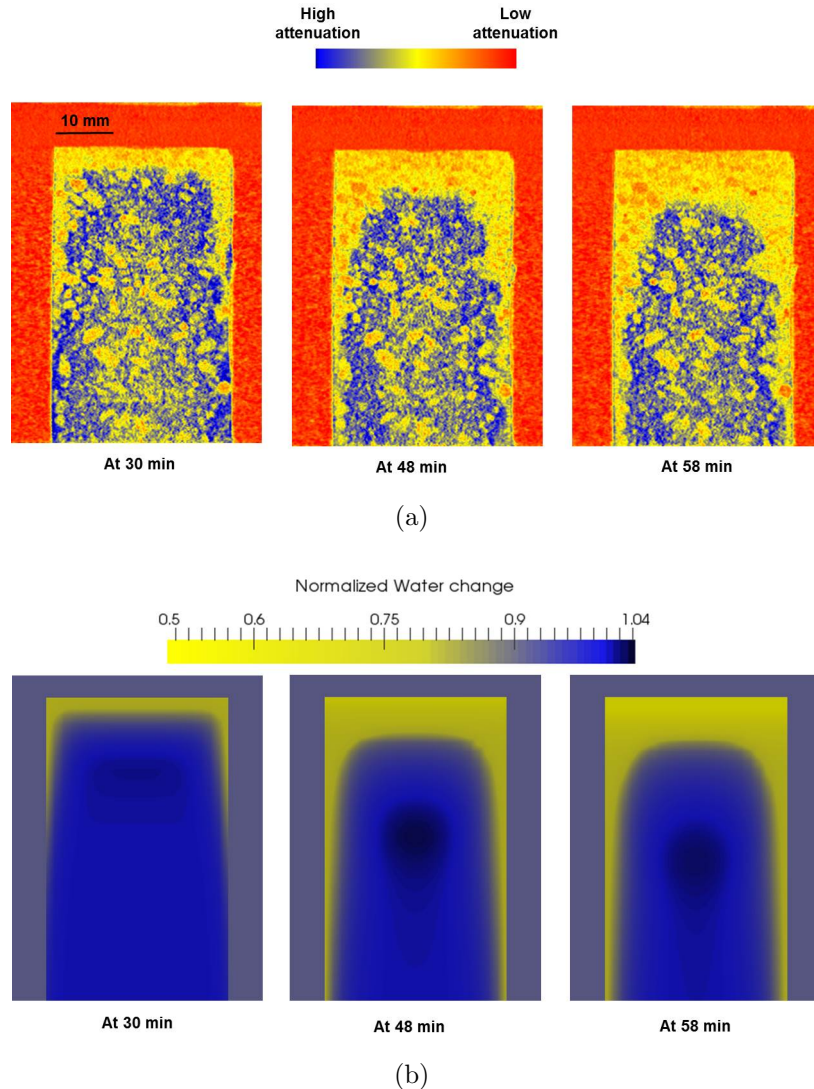


Figure 10: (a) Visualization of the variation of the water content measured by neutron imaging (b) Results of numerical simulations highlighting the shape of the drying front and the moisture accumulation

For a more quantitative comparison, moisture profiles are evaluated from the neutron tomography experiments. The attenuation coefficient (perceived in the images as a gray value) is directly related to the water content. Using this direct link, the vertical moisture profiles are obtained by sampling the average gray value in a disk-like probe region and scanning the depth of the sample at several instances in time. The probe is a few pixels high and includes only the core of the specimen, where the front is more uniform. The resulting profiles are normalized with respect to the initial moisture profile (see [10] for more details). This yields the vertical profiles shown in dotted lines in Figure 11. The horizontal plateau in the profiles correspond to the position of the drying front at each time step. These graphs can be interpreted as a quantitative representation of the images shown in Figure 10(a).

In numerical modeling, the variation in water content (w_{change}) is calculated from the change in the

saturation of pores and from dehydration of the cement paste:

$$w_{change} = (\phi S \rho_l)_0 - (\phi S \rho_l)_t + \Delta m_{dehyd} \quad (14)$$

The variation of the water content is normalized to the initial water content ($w_i = 189 \text{ kg/m}^3$ from the concrete mix) for direct comparison with the experimental results:

$$\hat{w}_{change} = \frac{w_i - w_{change}}{w_i} \quad (15)$$

As in the experimental curves, the normalized water change, \hat{w}_{change} , is computed in the core of the specimen for avoiding any boundary effect. The moisture profiles from the numerical model (solid lines) are compared with the experimental curves (dotted lines) in Figure 11.

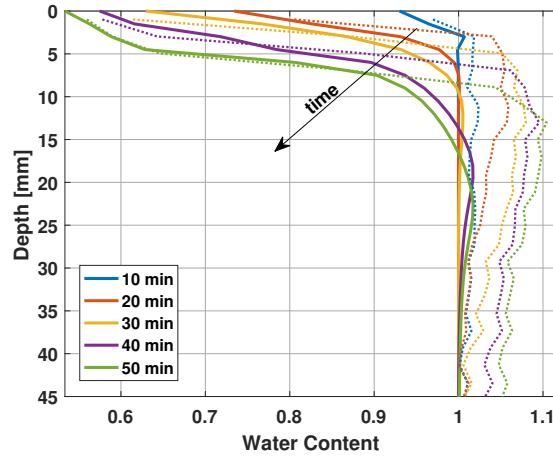


Figure 11: Case study 1: Moisture profile evolution: experimental (dotted lines) vs. numerical (solid lines)

The comparison shows that:

- The numerical model gives good results in terms of the speed and shape of the drying front. Despite some small discrepancies, the plateau of the drying front is well predicted.
- As it was visually shown in the results in Figure 10(b), moisture accumulation is observed behind the plateau of the drying front. This accumulation is more pronounced for profiles at 40 and 50 minutes. Quantitatively speaking, this moisture accumulation is much smaller than the one obtained from the neutron tomography images. However, as it was pointed out in [10], imaging artefacts such as beam hardening might affect the quantity of the moisture accumulation obtained from image analysis. This is discussed in more details in the following.

Discrepancies in the moisture accumulation

While the numerical model predicts very well the speed of the drying front, the moisture accumulation is considerably less than the one given by the neutron images. In [10], special attention has been given to the neutron tomography results regarding the moisture accumulation, as this phenomenon is often attributed to spalling of concrete. It has been shown that part of the apparent moisture accumulation might be an artefact of neutron beam hardening. The latter is an artifact occurring in X-ray and in neutron tomography. As a polychromatic beam passes through a sample, its mean energy increases (i.e., it becomes “harder”) because the lower-energy components are preferentially absorbed. The effect of beam hardening in neutron tomography is that the water content is underestimated in locations where the beam passes through a large thickness of water, i.e. near the axis of the cylinder. This phenomenon can be observed in Figure 10(a) where the sample seems to be dryer near the axis.

When looking at the change of water content, drying near the lateral surface reduces the effect of beam hardening, resulting in an apparent increase of water relative to the initial state. A simplified model for correcting the beam hardening effect has been presented in the Appendix A of [10].

This model showed that beam hardening, together with the lateral drying, makes the moisture accumulation appear more pronounced than it actually is in reality. As shown in Figure 12, after the beam hardening correction, the water accumulation is less.

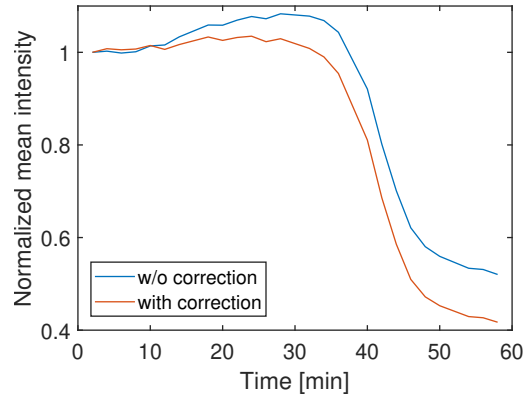


Figure 12: Evolution of intensity before and after beam hardening correction as given by a simplified model presented in [10]

The simplified correction model for beam hardening suggests that the real moisture accumulation is similar to the numerical result. Moreover, the model gives a more localized moisture accumulation, which seems to be more realistic than the one of the neutron images which appears to extend almost through the whole depth. In order to have a conclusive proof on the quantity of the moisture accumulation, more experiments are needed with improved boundary conditions. A perfect one-dimensional front would diminish the apparent increase in the moisture accumulation due to beam hardening, thus removing the need for correction.

4.3.3. Influence of boundary effect

In order to investigate the importance of lateral insulation, a perfect moisture insulation (no mass flux on the lateral sides) is assumed in the next simulation. The temperature results, compared in Figure 13 against experiments, are not different from the first case (see Figure 8).

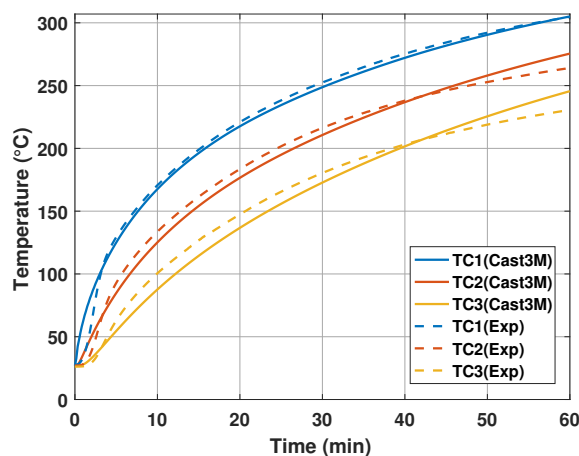


Figure 13: Case with perfect moisture insulation: Simulation of the temperature profiles across time measured by the three thermocouples (TC1, TC2, TC3) placed at three nominal positions (3, 10, and 20 mm from the heated surface)

The pressure field (Figure 14), in contrast to the previous case (see Figure 9), is uniform due to the fact that vapor is not allowed to escape on the sides.

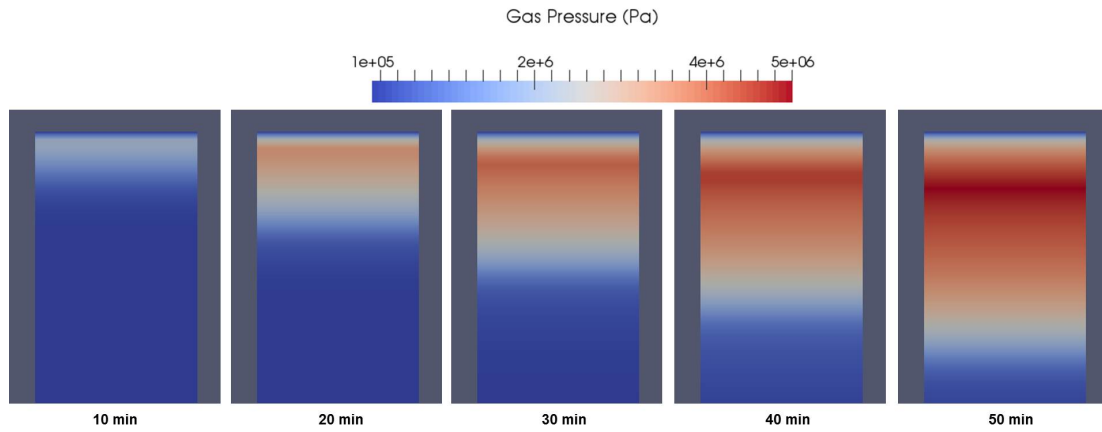


Figure 14: Case study with perfect moisture insulation: A uniform pressure field observed at different times

In Figure 15, the moisture profiles obtained from the case with perfect boundaries are compared with the ones obtained in the case of lateral moisture leak.

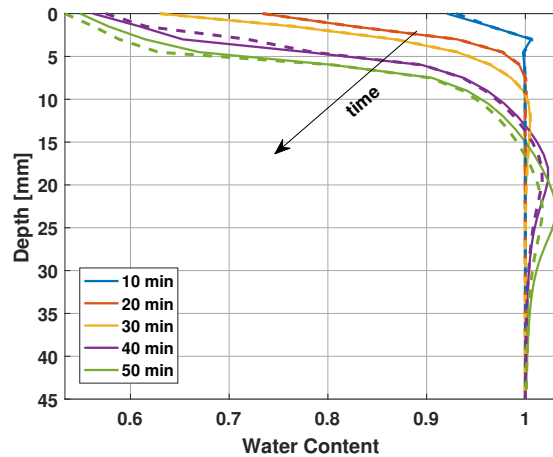


Figure 15: Numerical comparison of moisture profile evolution: perfect boundary (solid lines) vs. lateral moisture leak (dashed lines) highlighting the influence of lateral insulation

The boundary conditions do not have an important impact on the speed of the drying front, which is similar for the two cases. However, they influence the moisture accumulation behind the front, which is more pronounced in the case of perfect boundary conditions.

The water change at different times is shown in Figure 16. As one would expect, the front in this case is uniform. As observed in the profiles in Figure 15, insulation of the mass transfer on the sides results in a higher moisture accumulation. The latter does not concentrate only in the core of the sample, as in the first case study (see Figure 10(b)), but extends to the lateral sides of the specimen.

This numerical analysis shows the importance of having a better insulation in the experiments in order to obtain a unidimensional drying front for being as representative as possible to the real conditions in a heated structural element (*e.g.* wall, column etc.). It has been demonstrated numerically that the insulation has a direct influence on the quantity of the moisture accumulation, which is an important phenomenon probably linked to the mechanism of spalling.

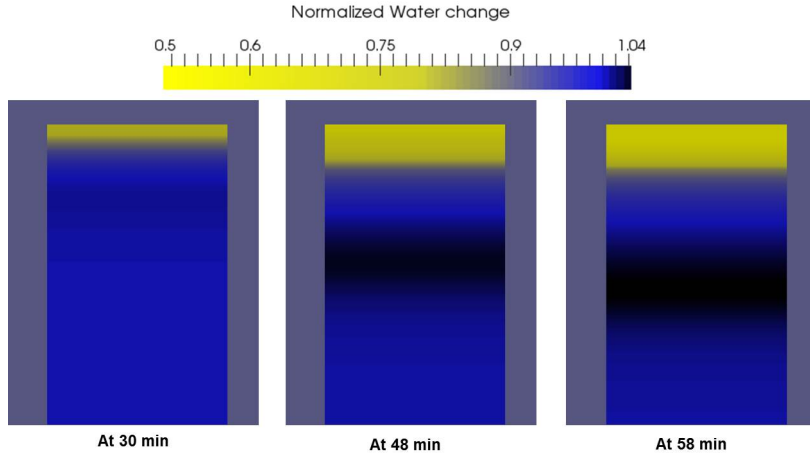


Figure 16: Case 2: Numerical simulation with no mass flux on the sides highlighting the uniformity of the drying front and higher moisture accumulation compared with Case 1

4.4. 3D simulations

In the previous section, 2D simulations of the front speed, the boundary effect and the moisture accumulation using a homogenized continuum model have been presented. In this section 3D simulations are performed for two reasons:

- First, for checking whether the 2D simulations, which have been performed in the previous section for simulating the front speed, are a good approximation for the boundary effect and the moisture accumulation or not. This numerical analysis is shown in the next section, where 3D simulations of HPC 4 mm, treated as a homogenized continuum, are performed.
- Second, 2D simulations are not enough for simulating the problem in mesoscale. As an example, 3D simulations are used for predicting the moisture profiles measured experimentally in a simplified case of a concrete sample HPC 4 mm with a single big aggregate. The objective is to use this simplified case to investigate the physical reasons for the faster drying front observed in concrete samples with bigger aggregates.

4.4.1. Homogeneous 3D model for HPC 4 mm

A cylindrical geometry with $d = 30$ mm and $h = 60$ mm is discretized in 2 mm tetrahedral elements of first order as shown in Figure 17. For building the FE mesh, Salome [31], which is an open source platform, has been used. Then the mesh is imported in Cast3M.

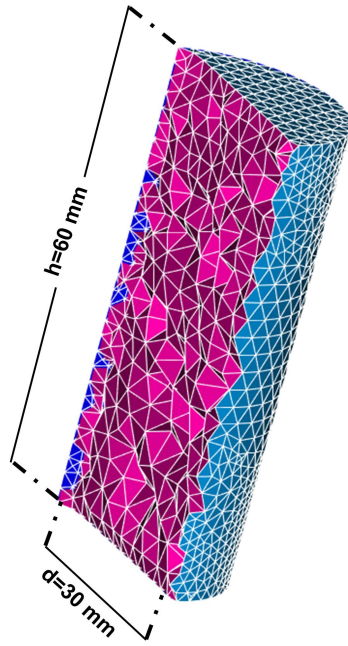


Figure 17: Finite element mesh generated in Salome

The pressure field is shown in Figure 18. The variation of the water content is visualized in Figure 19. The results of this study are very similar (not to say identical) with the 2D simulations (see Section 4.3). Therefore it can be concluded that a 2D model is sufficient for the simulations of temperature, gas pressure and moisture content when a homogenized continuum model is adopted.

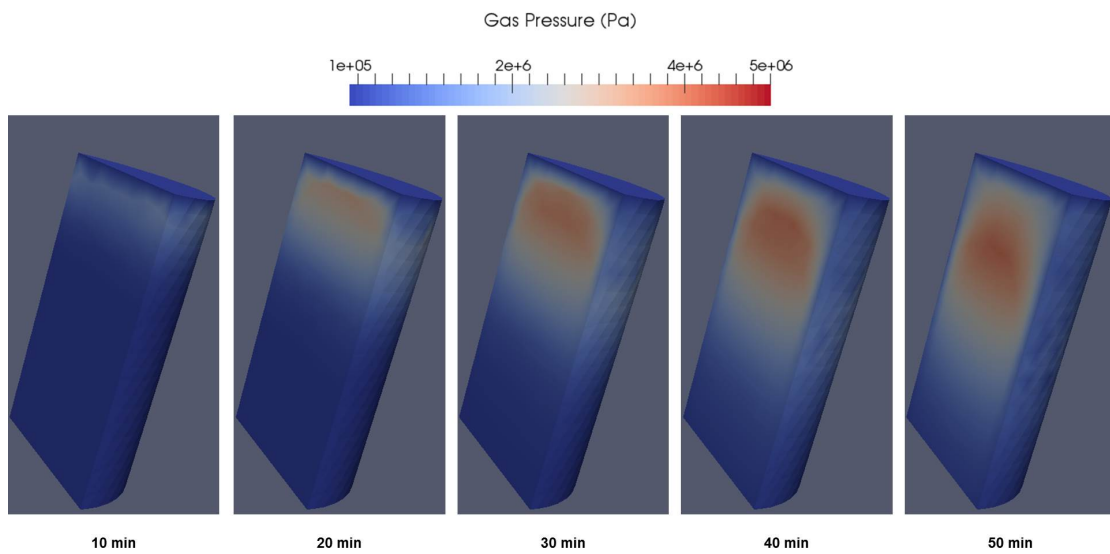


Figure 18: 3D simulations of HPC 4mm

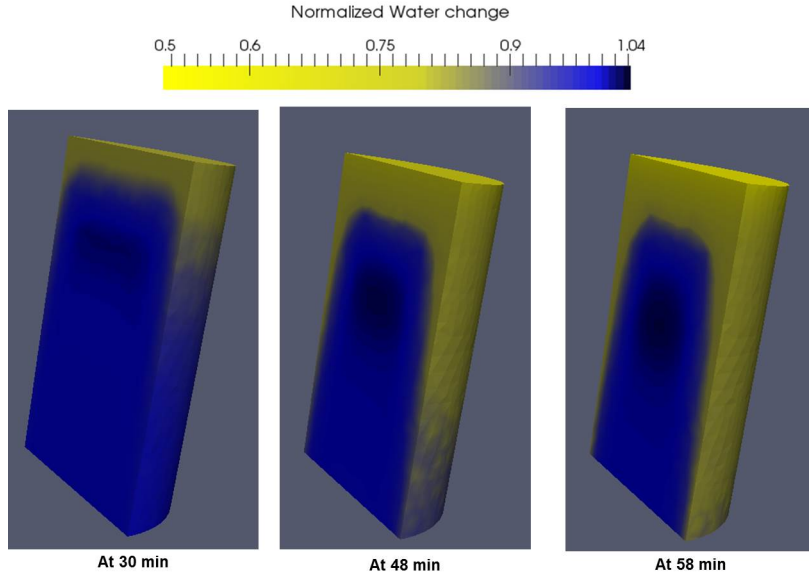


Figure 19: Water Content from 3D simulations

4.4.2. Mesoscopic approach: Influence of a single aggregate

In this section, mesoscopic modeling of the moisture distribution in HPC 4 mm with a single aggregate at the top is presented. For the sample under consideration, the moisture distribution has been measured experimentally by neutron tomography ([10]). In contrast to the analysis presented in Section 4.4.1, where a homogenized continuum model is used, a mesoscopic approach is adopted here. In other words, the single aggregate and cementitious matrix are considered explicitly in the numerical model. First, only the thermo-hydral behavior is considered (Section 4.4.2.1). Then the mechanical behavior is also included in the simulations (Section 4.4.2.2).

4.4.2.1. TH simulations.

The single aggregate inside the HPC 4 mm sample has the shape of a spheroid. The dimensions and the exact position of the aggregate have been measured from the images and are used for constructing the geometry in the numerical model. The dimensions of the spheroid representing the aggregate are shown in Figure 20. The aggregate is modeled as a solid material (no permeability, no porosity) with a higher thermal conductivity (about 3 times) with respect to the cementitious matrix ($\lambda_a = 6.28 \frac{\text{W}}{\text{m}\cdot\text{K}}$ as measured in [32]). Thus the aggregate will transfer heat but not mass. It should be noted that the experimental characterization of the constituents (*i.e.*, aggregates and cementitious matrix) of the tested concrete is missing. Therefore, the thermo-hydral material properties of each constituent has been retrieved from literature, mainly from [32].

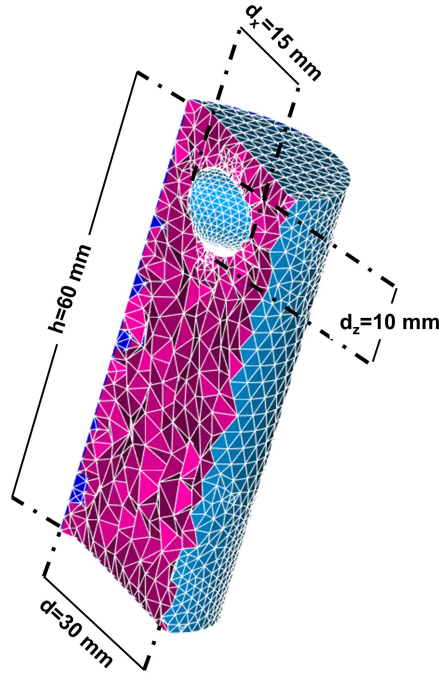


Figure 20: Finite element mesh highlighting the single aggregate at the top

In order to have a closer look at the influence of the aggregate on the thermal field, the temperatures along the width of the sample at 20 mm from the heated surface, just below the single aggregate, are compared in Figure 21.

For the homogeneous case (solid line), it is observed that the temperature is slightly higher at the core than at the outside. This is due to the drying at the boundaries which influences the temperature field through the latent heat. As more water is evaporated near the boundary, the temperature propagation is delayed due to the consumption of energy which takes place in evaporation. However, quantitatively this effect is negligible (less than 1°C). When looking at the same profile in HPC 4 mm with a single aggregate, a more pronounced increase of temperature at the core of the specimen is observed. This is due to the higher conductivity of aggregate compared to the cementitious matrix. The difference between the two cases is less than 4°C .

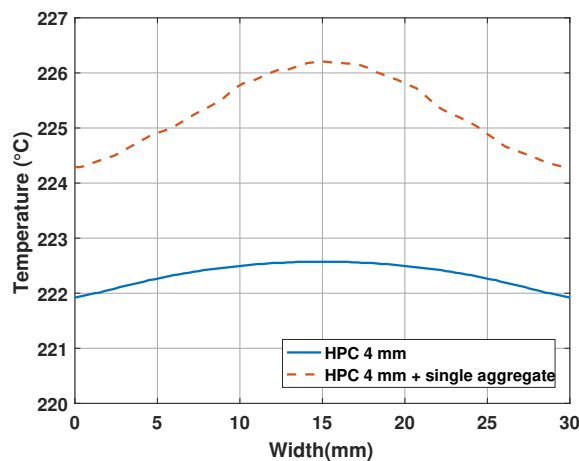


Figure 21: Temperature along the width of the specimen at a distance 20 mm from the heated surface (just below the aggregate) after 60 min of heating

The pressure field is presented in Figure 22 and pressure profiles at 20 mm from the heated surface are compared in Figure 23. The pressure obtained from the mesoscale model is higher than the one

obtained from the homogenous model, because of the additional flow resistance due to the single aggregate.

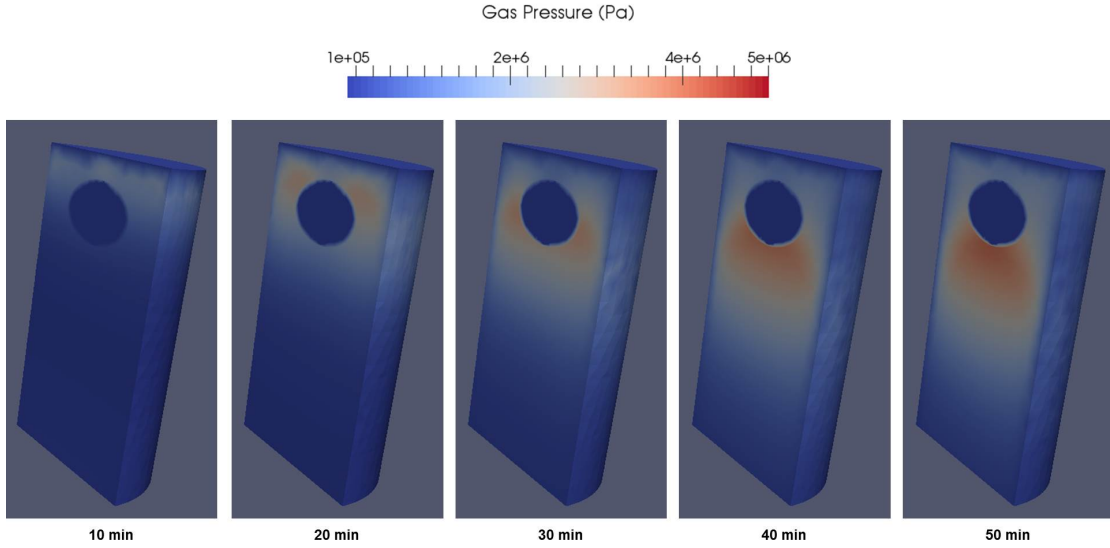


Figure 22: 3D simulations of pressure field in HPC 4 mm with a single big aggregate

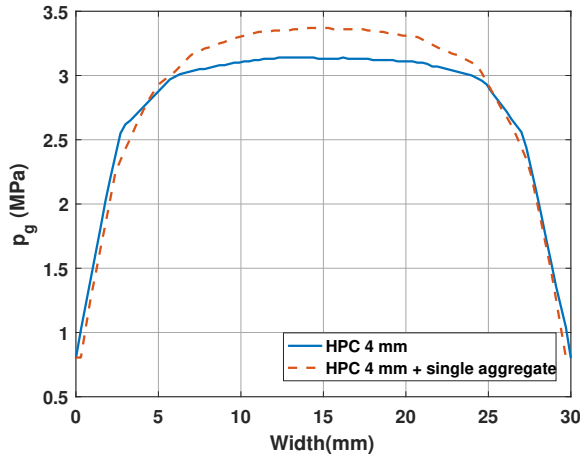


Figure 23: Pressure along the width of the specimen at a distance 20 mm from the heated surface (just below the aggregate) after 60 min of heating

The evolution of the moisture content given by the neutron tomography is shown in Figure 24(a) and the results from the numerical simulations in Figure 24(b).

In these numerical results it is observed that:

- The speed of the drying front is the same as in the homogeneous case (see Figure 19). In contrast to the experiment, no direct influence of the aggregate on the drying front can be seen. In the experiments (see Figure 24(a)), the drying process is accelerated around the aggregate. This phenomenon is not captured by the numerical model. Indeed, the fracture network, which is likely to be more pervasive around the aggregate, may result in a faster drying around the aggregate. This physical process is considered in the next section.
- A smaller water accumulation (black color in the interior) with respect to the homogeneous case is observed (see Figure 19). Due to the presence of the big aggregate, the vapor source coming from phase changes of cement is lower. Therefore, the vapor condensation toward the cooler side is less.

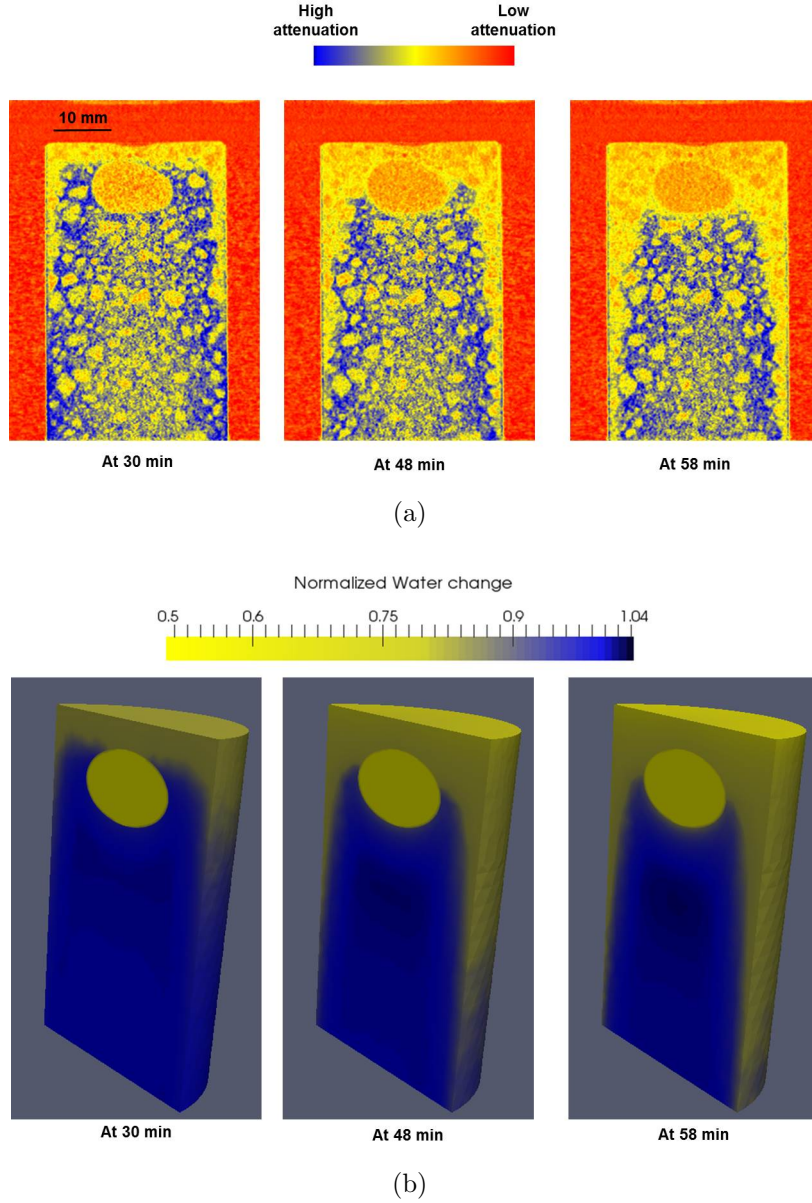


Figure 24: Evolution of moisture content: (a) Experiments (b) Numerical Model

4.4.2.2. THM simulations with damage-permeability coupling.

To capture the faster drying around the aggregate, which is likely to be caused by a more pervasive fracture network around the aggregate, THM simulations are performed in this section.

To prevent softening and localization issues, stresses at a material point shall not be described locally, but must take into account the interaction between defects (pores, microcracks) at the microstructural level. Therefore, a non-local damage mechanical model [33] is used for the mechanical part. The nonlocal theory applied to damage mechanics consists of averaging a mechanical quantity in its neighborhood using Gaussian weight functions. The characteristic size of the weighting domain depends on the characteristic length l_c which is linked to the size of material heterogeneity. The characteristic length used in these simulations is three times the diameter of heterogeneity in the cement paste ($l_c = 3d_a$) as in [33].

The damage parameter is coupled with the permeability of the material as in [29]:

$$k = k_0 \cdot 10^{A_T(T-T_0)} \cdot \left(\frac{p_g}{p_{atm}} \right)^{A_p} \cdot 10^{A_d d} \quad (16)$$

where $k_0=10^{-20} \text{ m}^2$, $A_T = 0.005$, $A_p = 0.368$. Different values exist in literature for the damage coefficient A_d [29, 34, 35]. In the present paper, A_d was taken 1, as this value was found to fit best the high-temperature measurements in [34].

The damage field is presented in Figure 25(a). Similar to what has been already postulated in literature [6], damage in the cementitious matrix around the aggregate is observed due to the different thermal behavior of the concrete components at high temperature.

The evolution of the moisture content is presented in Figure 25(b). The much higher permeability induced by damage seems to influence the shape of the drying front.

Such a result can be used for the interpretation of the faster drying of samples with bigger aggregates (see Figure 3). In a case where a number of big aggregates are found in a concrete sample, such as in HPC 8 mm, it can be imagined that the damage induced in the cementitious matrix around the assembly of aggregates, influences the global speed of the drying front. However, the example with the single aggregate is not enough as a conclusive proof for explaining the faster drying front observed experimentally on samples with bigger aggregate size. Nevertheless, the analysis of the single aggregate remains a good proof of concept and is an important first step towards 3D mesoscopic numerical analysis that considers the full particle size distribution of concrete.

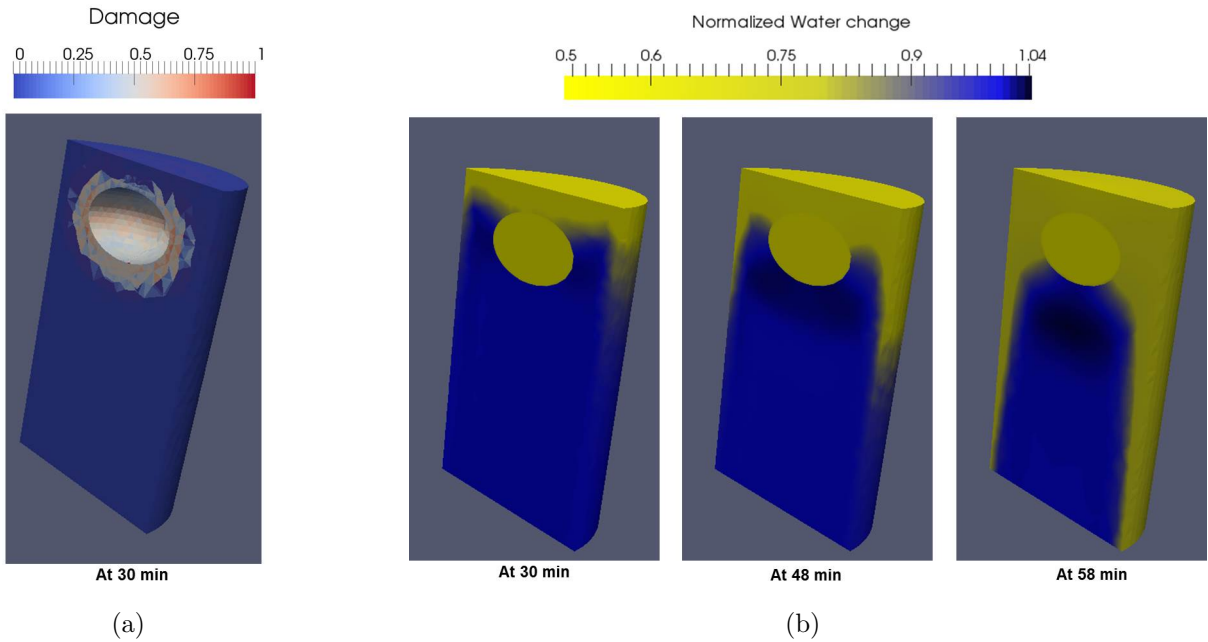


Figure 25: (a) Damage field and (b) evolution of water content highlighting the influence of single aggregate

5. Conclusions

In this paper, a numerical model implemented in Cast3M has been used for simulating neutron tomography experiments on heated concrete.

The model uses adjusted constitutive laws from previous neutron radiography tests performed on the same concrete material, but on a sample with different geometry and size, as well different heating method (*i.e.*, radiator vs. thermal plate).

The model gives a good prediction of the drying speed. It also predicts a moisture accumulation, which is, however, less than the one observed in the neutron images. But one has to keep in mind

that neutron images can be altered by artefacts. Indeed, a simplified image analysis has shown that, due to the lateral drying, beam hardening makes the moisture accumulation appear more pronounced than it actually is. However, more experiments with improved boundary conditions are needed for a conclusive proof on the quantity of the moisture accumulation.

When a mass flux boundary condition is applied laterally, the model is also able to capture the additional lateral drying observed experimentally. This result suggests that the reason for the boundary effect is the insufficient moisture insulation in the lateral surface.

The importance of boundary conditions has been investigated through a numerical analysis comparing two cases: perfect vs. imperfect moisture insulation. It was found out that there is no difference in the speed of the drying front. However, imperfect moisture insulation results in a lower moisture accumulation.

The predictive capabilities of the model, after having calibrated the constitutive behavior of the material from a previous different experiment, with no additional parameter tuning involved, shows that it can be a useful tool for investigating the physical phenomena in heated concrete.

A 3D mesoscopic simulation of the experiment with a single big aggregate at the top has been performed for the purpose of investigating the influence of the aggregate size on the drying front. Thermo-hydro-mechanical simulations showed that the damage of the cementitious matrix around the aggregates influences the shape of the drying front. No influence of the aggregate on the drying front was observed, when damage was excluded from the model. Such a result is an important step towards the physical interpretation of the faster drying in samples with bigger aggregate size, but can not be considered as a conclusive proof. Nevertheless, it opens the way to 3D THM mesoscopic numerical analysis that considers a real concrete mesoscopic structure, which could possibly confirm the difference in drying speed.

Acknowledgements

This study was partially financed by LabEx TEC21.

References

References

- [1] D. Gawin, C. Majorana, B. Schrefler, Numerical analysis of hygro-thermal behaviour and damage of concrete at high temperature, *Mechanics of Cohesive-frictional Materials* 4 (1) (1999) 37–74.
- [2] S. Dal Pont, H. Colina, A. Dupas, A. Ehrlicher, An experimental relationship between complete liquid saturation and violent damage in concrete submitted to high temperature, *Magazine of Concrete Research* 57 (8) (2005) 455–461.
- [3] R. Tenchev, L. Ly, J. Purkiss, Finite element analysis of coupled heat and moisture transfer in concrete subjected to fire, *Numerical Heat Transfer Part A-applications* 39 (2001) 685–710.
- [4] C. T. Davie, C. J. Pearce, N. Bićanić, Coupled heat and moisture transport in concrete at elevated temperatures - effects of capillary pressure and adsorbed water, *Numerical Heat Transfer, Part A: Applications* 49 (8) (2006) 733–763.
- [5] P. Kalifa, F.-D. Menneteau, D. Quenard, Spalling and pore pressure in HPC at high temperatures, *Cement and Concrete Research* 30 (12) (2000) 1915 – 1927.
- [6] J.-C. Mindeguia, Experimental contribution to the understanding of the thermal instability risk of concrete, *Theses, Université de Pau et des Pays de l'Adour* (Jul. 2009).
- [7] B. Weber, M. Wyrzykowski, M. Griffa, S. Carl, E. Lehmann, P. Lura, Neutron radiography of heated high-performance mortar, *MATEC Web of Conferences* 6 (2013) 03004.
- [8] N. Toropovs, F. Lo Monte, M. Wyrzykowski, B. Weber, G. Sahmenko, P. Vontobel, R. Felicetti, P. Lura, Real-time measurements of temperature, pressure and moisture profiles in high-performance concrete exposed to high temperatures during neutron radiography imaging, *Cement and Concrete Research* 68 (2015) 166 – 173.
- [9] D. Dauti, S. Dal Pont, B. Weber, M. Briffaut, N. Toropovs, M. Wyrzykowski, G. Sciumé, Modeling concrete exposed to high temperature: Impact of dehydration and retention curves on moisture migration, *International Journal for Numerical and Analytical Methods in Geomechanics* 42 (13) (2018) 1516–1530.
- [10] D. Dauti, A. Tengattini, S. Dal Pont, N. Toropovs, M. Briffaut, B. Weber, Analysis of moisture migration in concrete at high temperature through in-situ neutron tomography, *Cement and Concrete Research* 111 (2018) 41 – 55.
- [11] G. Xotta, G. Mazzucco, V. Salomoni, C. Majorana, K. Willam, Composite behavior of concrete materials under high temperatures, *International Journal of Solids and Structures* 64-65 (2015) 86 – 99.
- [12] M. Hassanizadeh, W. G. Gray, General conservation equations for multi-phase systems: 1. averaging procedure, *Advances in Water Resources* 2 (1979) 131 – 144.
- [13] M. Hassanizadeh, W. G. Gray, General conservation equations for multi-phase systems: 2. mass, momenta, energy, and entropy equations, *Advances in Water Resources* 2 (1979) 191 – 203.
- [14] M. Hassanizadeh, W. G. Gray, General conservation equations for multi-phase systems: 3. constitutive theory for porous media flow, *Advances in Water Resources* 3 (1) (1980) 25 – 40.
- [15] R. W. Lewis, B. A. Schrefler, *The Finite Element Method in the Static and Dynamic Deformation and Consolidation of Porous Media*, John Wiley, 1998.
- [16] F. Pesavento, Nonlinear modelling of concrete as a multiphase material in high temperature conditions, Ph.D. thesis, *Universita degli Studi di Padova* (2000).
- [17] B. A. Schrefler, C. E. Majorana, G. A. Houry, D. Gawin, Thermo-hydro-mechanical modelling of high performance concrete at high temperatures, *Engineering Computations* 19 (7) (2002) 787–819.
- [18] D. Gawin, F. Pesavento, B. Schrefler, Modelling of hygro-thermal behaviour of concrete at high temperature with thermo-chemical and mechanical material degradation, *Computer Methods in Applied Mechanics and Engineering* 192 (13–14) (2003) 1731 – 1771.
- [19] S. Dal Pont, S. Durand, B. Schrefler, A multiphase thermo-hydro-mechanical model for concrete at high temperatures—finite element implementation and validation under {LOCA} load, *Nuclear Engineering and Design* 237 (22) (2007) 2137 – 2150.
- [20] S. Dal Pont, F. Meftah, B. Schrefler, Modeling concrete under severe conditions as a multiphase material, *Nuclear Engineering and Design* 241 (3) (2011) 562 – 572.
- [21] G. Sciumè, F. Benboujema, C. De Sa, F. Pesavento, Y. Birtaud, A multiphysics model for concrete at early age applied to repairs problems, *Engineering Structures* 57 (2013) 374 – 387.
- [22] CEA, Cast3M 15.0, Finite Element Software, <http://www-cast3m.cea.fr/index.php> (2006).
- [23] T. Harmathy, L. Allen, Thermal properties of selected masonry unit concretes, *Journal of American Concrete Institute* 70.
- [24] Z. Bažant, M. Kaplan, *Concrete at High Temperatures: Material Properties and Mathematical Models*, Concrete design and construction series, Longman, 1996.
- [25] I. Hager, Comportement à haute température des bétons à haute performance: évolution des principales propriétés mécaniques, Ph.D. thesis, *Marne-la-Vallée, ENPC* (2004).

- [26] D. Dauti, S. Dal Pont, M. Briffaut, G. Sciumé, Numerical benchmark of experiments on heated concrete, in: 5th International Workshop on Concrete Spalling due to Fire Exposure in Boras, Sweden, 2017, pp. 197–203.
- [27] D. Dauti, A combined experimental and numerical approach to spalling of high performance concrete due to fire, Ph.D. thesis, Université Grenoble Alpes (2018).
- [28] F. Meftah, S. Dal Pont, Staggered finite volume modeling of transport phenomena in porous materials with convective boundary conditions., *Transport in Porous Media* 82 (2) (2010) 275 – 298.
- [29] D. Gawin, F. Pesavento, B. A. Schrefler, Simulation of damage-permeability coupling in hygro-thermo-mechanical analysis of concrete at high temperature, *Communications in Numerical Methods in Engineering* 18 (2) (2002) 113–119.
- [30] D. Gawin, F. Pesavento, B. A. Schrefler, Modelling of hygro-thermal behaviour and damage of concrete at temperature above the critical point of water, *International Journal for Numerical and Analytical Methods in Geomechanics* 26 (6) (2002) 537–562.
- [31] A. Ribes, C. Caremoli, Salome platform component model for numerical simulation, in: 31st Annual International Computer Software and Applications Conference (COMPSAC 2007), Vol. 2, 2007, pp. 553–564.
- [32] T. Harmathy, Thermal Properties of Concrete at Elevated Temperatures, Research paper, National Research Council of Canada, 1970.
- [33] G. Pijaudier-Cabot, Z. Bažant, Nonlocal damage theory, *Journal of Engineering Mechanics - ASCE* 113 (10) (1987) 1512–1533.
- [34] S. Dal Pont, A. Ehrlacher, Numerical and experimental analysis of chemical dehydration, heat and mass transfers in a concrete hollow cylinder submitted to high temperatures, *International Journal of Heat and Mass Transfer* 47 (1) (2004) 135 – 147.
- [35] B. Bary, Etude du couplage hydraulique-mécanique dans le béton endommagé, Ph.D. thesis, école normale supérieure (1996).